Design, Fabrication, and Characterization of a 240 × 240 MEMS Uncooled Infrared Focal Plane Array With 42-μm Pitch Pixels

Yi Ou, Zhigang Li, Fengliang Dong, Dapeng Chen, Qingchuan Zhang, and Changqing Xie

***Abstract*—We report a significant step in the design, fabrication, and performance evaluation of a 240 × 240 microelectromechanical system uncooled infrared (IR) focal plane array (FPA) with 42-μm pitch pixels. An improved analytical model has been developed to optimize the design. The optimal key parameters have been verified through experiments, including thermal transmission efficiency, thermomechanical sensitivity, thermal sensitivity, and response time. Compared with our previous work, the number of the fabricated FPA's pixels is increased by 125% and the corresponding pixel's area is decreased by 51%. Furthermore, our FPA has a good sensitivity with a noise equivalent temperature difference of about 373 mK, thus providing an extension of state-of-the-art IR FPA and practical information for future applications. [2012-0226]**

***Index Terms*—Focal plane array (FPA), infrared (IR) imaging, microfabrication process, optical readout, response time, vacuum package.**

I. Introduction

INFRARED (IR) imaging in the spectral regions ranging from 8–14 μm has attracted much attention in recent years due to its outstanding properties for night vision, remote sensing, and driving aids applications. Traditional thermal IR imaging devices, in which the temperature rise on each pixel is electrically measured by changes in either resistance or capacitance, have been already commercialized due to their compatibility with electric signal processing. The studies on IR focal plane array (FPA) sensors with electrical readout have been carried out extensively. For example, Wada and Nagashima reported a vanadium oxide detector of 256 × 256 at a pitch of 50 μm with a noise equivalent temperature difference (NETD) of 150 mK [1]. Tissot *et al.* reported a 640 × 480 uncooled amorphous silicon IR FPA with 25-μm pixel pitch [2]. They have achieved excellent properties, but several issues still need to be solved, such as thermal noise from the readout circuit and fabrication complexity.

Microelectromechanical system (MEMS)-based IR FPA with an optical readout system offers an alternative method to enhance IR imaging performance. In particular, an optical readout method can reduce thermal noise caused by a readout circuit dramatically and the fabrication complexity. Along with its other advantages such as ease of use, cost efficiency, and long-term stability, optical readout method has a great potential with the rapid development of MEMS technology. The theoretical NETD of MEMS-based IR FPA with an optical readout system can be as low as 5 mK [3], with an expense of low image resolution. In other words, the tradeoff between absorption area of pixel and NETD should be carefully treated. The NETD of MEMS-based IR FPA with an optical readout system is determined by the total noise level of the system, including the thermodynamic fluctuation noise, vibration noise, temperature stability, and optical readout noise.

The principle of MEMS-based IR FPA with an optical readout system incorporates serpentine bimaterial cantilevers, which are often used as sensitive components. When incident IR radiation is absorbed, the deflection induced by the bimaterial effect [3] can be detected by the optical readout system and translated into a visible image.

MEMS-based IR FPA using bimaterial microcantilever structures has been proven to be very effective in IR imaging. Hunter *et al.* introduced a capacitive plate based on bimaterial microcantilevers, whose position is sensitive to temperature change, and the capacitance is coupled to the input of a low-noise complementary metal–oxide–semiconductor readout integrated circuit. With this technology, a prototype of 160 × 120 FPA with 50-μm pixel pitch was demonstrated [4]. Lavrik *et al.* reported the fabrication and performance of a 256 × 256 MEMS IR FPA [5]. Grbovic *et al.* demonstrated an uncooled IR imaging array. The NETD and the response time of the implemented MEMS-based IR detector were measured to be as low as 0.5 K and 6 ms, respectively [6]. A bimaterial cantilever-based MEMS FPA of 160 × 120 pixels has been also presented by Yu *et al.* The NETD was theoretically estimated to be below 60 mK, and the response time was calculated to be 15 ms [7].

The author group has developed the freestanding bimaterial cantilever FPA for IR imaging using an optical readout system

Manuscript received August 6, 2012; revised September 26, 2012; accepted October 22, 2012. Date of publication November 26, 2012; date of current version March 29, 2013. This work was supported in part by the National Natural Science Foundation of China under Grant 61274119 and in part by the Opening Project of the Key Laboratory of Microelectronics Devices and Integrated Technology, Institute of Microelectronics, Chinese Academy of Sciences. Subject Editor X. Zhang.

Y. Ou, Z. Li, D. Chen, and C. Xie are with the Key Laboratory of Microelectronics Devices and Integrated Technology, Institute of Microelectronics, Chinese Academy of Sciences, Beijing 100029, China (e-mail: ouyi@ime.ac.cn; dpchen@ime.ac.cn; xiechangqing@ime.ac.cn).

F. Dong is with the National Center for Nanoscience and Technology, Beijing 100190, China.

Q. Zhang is with the CAS Key Laboratory of Mechanical Behavior and Design of Materials, University of Science and Technology of China, Hefei 230027, China (e-mail: zhangqc@ustc.edu.cn).

Color versions of one or more of the figures in this paper are available online at http://ieeexplore.ieee.org.

Digital Object Identifier 10.1109/JMEMS.2012.2227140

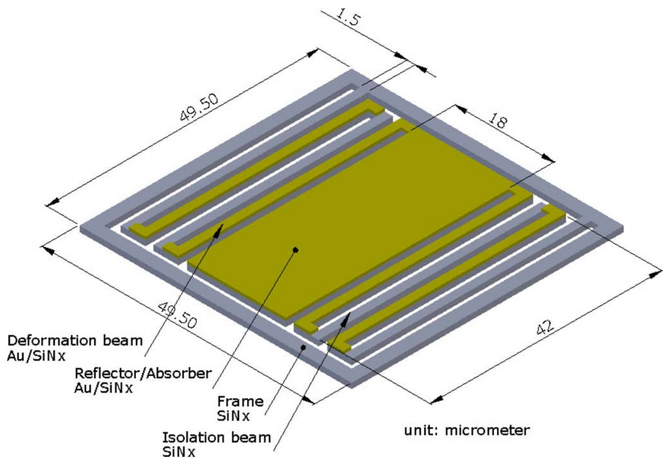

Fig. 1. Schematic geometry of an FPA's pixel (unit: micrometer). The pixel of the FPA consists of a composite film of SiN_x and Au layers having an absorption/reflection area of 42 μm × 18 μm.

with some promising results. In the previous work, a 200 × 200 FPA with pixel size of 184 μm × 136 μm [8], a 160 × 160 FPA with pixel size of 120 μm × 120 μm and NETD of 400 mK [9], and a 160 × 160 FPA with pixel size of 60 μm × 60 μm and NETD of 330 mK [10] have been reported. The main limiting factor for further miniaturization of the MEMS uncooled IR FPA has been the pixel size. In this paper, we present the development of the design, fabrication, and performance evaluation of a 240 × 240 MEMS uncooled IR FPA with 42-μm pixel pitch. Compared with our previous results, the pixel number is increased by 125% and the corresponding pixel area is decreased by 51%. More importantly, no significant decrease in NETD is observed. It should be noted that the design of IR FPA with such a small pixel is a challenging task due to the fact that the tradeoff between the absorption area of pixel and NETD needs to be carefully considered. The analyses of IR FPA in this paper eventually provide practical information for future applications.

II. Principle

The key element of the IR FPA is the pixel, as illustrated in Fig. 1. The cantilever structure consists of a reflector/absorber and multifolded interval metallized beams. The reflector deflects as a bimaterial beam bends due to the difference of thermal expansion coefficients when temperature of the beam rises. The magnitude of the deflection of all pixels can be measured by an optical system using visible probing light, and the resulting visible images of the detected object are captured by a charge-coupled device (CCD) [11], [12]. The purpose of interval metallization on the beam is to form the thermal isolation beam, leading to the reduction of heat loss along the beam and the increase in heat accumulation on the absorber.

According to the basic principle of FPA, to improve the FPA's performance, the key performance parameters, including thermal transmission efficiency, thermomechanical sensitivity, thermal sensitivity, and response time [1], should be optimized to avoid losing thermal sensitivity, which can be induced due to the decrease in absorption area on each pixel. In other words, the goal of this paper is to maximize the pixel's temperature rise and optimize the thermomechanical response for a given incident IR radiation under the constraints of predetermined pixel size. In addition, the response time and vacuum packaging should be also considered, which will be discussed in detail in the following sections.

A. Thermal Transmission Efficiency

Thermal transmission efficiency H is defined as the ratio of the temperature rise ΔT on the reflector to the temperature rise ΔT_s of the IR source, which indicates the FPA's capability to sense the temperature difference between a target and the background. Considering a pixel in the FPA at thermal equilibrium with surroundings, there are four kinds of ways to exchange heat within or between FPA's pixels, namely, conduction of pixel's beams, conduction between pixels, convection and conduction of air, and finally, radiation of a pixel. Thereby, the FPA's thermal transmission efficiency can be expressed as [13]

$$H = \frac{\Delta T}{\Delta T_s} = \frac{A_e \varepsilon \gamma \pi}{4F^2(G_{\text{cond}} + G_{\text{rad}} + G_{\text{air}})} \times \frac{dP}{dT_0} \qquad (1)$$

where A_e is the pixel's absorption area; ε is the emissivity of the pixel $(= 0.8)$; and γ and F are the transmissivity $(= 0.9)$ and F number of the IR lens $(= 0.8)$, respectively. dP/dT_0 is the fraction of the radiative energy emitted by the source at temperature T_0 (300 K) and is equal to 0.63 $W/\text{m}^2 \cdot \text{sr} \cdot \text{K}$ ranging from 8 to 14-μm spectral band. G_{cond}, G_{rad}, and G_{air} denote the thermal conductivity of beams, thermal radiation, and conductivity of air, respectively. Here, G_{air} can be ignored since FPA is designed to package under vacuum. G_{rad} and G_{cond} are expressed as

$$\begin{aligned} G_{\text{rad}} &= 4\sigma A_{\text{pixel}}(\varepsilon_1 + \varepsilon_2)T_0^3 \\ G_{\text{cond}} &= 2\left[\frac{nL}{\mu_1 A_1 + \mu_2 A_2} + \frac{nL}{\mu_2 A_2}\right]^{-1} \end{aligned} \qquad (2)$$

where σ is Boltzmann's constant, A_{pixel} is the total area of the pixel, μ is the thermal conductivity, n is the folded number of beams, L is the beam length, and A is the cross-sectional area of layers. Subscripts 1 and 2 represent the reflector and absorber layers, respectively. The same subscripts are also used for other following parameters.

From (1) and (2), one can see that lowering the thermal conductivity can help to improve FPA's sensitivity. Therefore, it is important to design the supporting beam structure of the pixel with large length and small cross-sectional area and choose a material with low thermal conductivity.

B. Thermomechanical Sensitivity

After IR radiation is absorbed by the absorber layer, deformation of the bimaterial beams causes the reflector to deflect. Thermomechanical sensitivity is defined as the deflection angle in relation to temperature change on the pixel and can be given by the integration of beam curvature [14], [15]

$$S = \frac{\theta}{\Delta T} = 6(\alpha_1 - \alpha_2)\left(\frac{t_1/t_2+1}{t_2 D}\right) L\frac{n+1}{2} \quad (3)$$

where α is the thermal expansion coefficient; t is the thicknesses of two layers of bimaterial cantilever with length of L; and D is a structure constant containing layer thickness, elastic module, and Poisson's ratio. It can be seen from (3), to improve thermomechanical sensitivity S, the thickness of t_2 should be minimized as L and n can only be regulated in some range due to restriction of pixel sizes. Materials with larger mismatch in thermal expansion coefficients should be also chosen to improve S.

C. Thermal Sensitivity

After the reflectors are deflected, a CCD in the optical readout system is employed to detect the gray level change caused by the deflection angle of the reflector. Thus, CCD's gray level change reflects FPA's sensitivity R, which can be written in terms of thermal transmission efficiency H, thermomechanical sensitivity S, and minimum detectable deflection angle $\theta_{\min}$

$$R = \frac{H \times S}{\theta_{\min}} = 6(\alpha_1 - \alpha_2)\left(\frac{t_1/t_2+1}{t_2 D}\right)\cdot\frac{n+1}{2} \times \frac{A_e \varepsilon \gamma \pi}{4F^2(G_{\text{cond}} + G_{\text{rad}} + G_{\text{air}})} \cdot \frac{dP}{dT_0} \cdot \frac{1}{\theta_{\min}} \quad (4)$$

where $\theta_{\min} = \lambda/2LN$ is determined by the grayscale of the CCD (here, $N = 12$ bit), the wavelength of the probing light λ, and the length of the reflector L. Equation (4) shows that larger values of S and H are expected to increase R; on the other hand, R is inversely proportional to $\theta_{\min}$, which can be decreased by choosing a CCD with a higher grayscale or the probing light with a smaller wavelength, since L is limited.

D. Response Time

The thermal response time is the period that is from the point where the thermal exchange starts to the point where the thermal exchange reaches equilibrium. When the IR object is removed, the time taken by pixel's reflector to restore its initial position due to mechanical spring force of the beams is defined as mechanical response time. The thermal response time is a key issue to determine FPA's response time because it governs the FPA's response to an IR object.

Part One—Thermal Response Time: As aforementioned, heat can be exchanged by thermal conduction of pixel's cantilevers, frame's thermal conduction, convection and conduction of air, and radiation of the pixel. Thereby, the FPA's thermal response time is determined by the pixel's heat capacitance and thermal conductivity

$$\xi(t) = \frac{\rho_1 V_1 c_1 + \rho_2 V_2 c_2}{G_{\text{rad}} + G_{\text{cond}} + G_{\text{air}}} \quad (5)$$

where ρ, V, and c respectively denote the density, volume, and thermal capacitance of a bimaterial cantilever. In (5), the air thermal convection and conduction can be ignored because the FPA is encapsulated under very low air pressure. Regarding the thermal conduction G_{cond}, previous research studies only considered it within a single pixel [3], [9], [15] and neglected thermal conduction of the frame. This leads to the difference between simulation and experimental outcomes. Because heat conducts from a pixel to the frame along with the cantilevers, for a heated pixel, G_{cond} in (2) should be corrected by frame's thermal conductance

$$G_f = \mu_2 A_f / L_f. \quad (6)$$

Then, the total conductance in (2) is rewritten as

$$G_{\text{cond}} = 2\left[\frac{nL}{\mu_1 A_1 + \mu_2 A_2} + \frac{nL}{\mu_2 A_2} + \frac{L_f}{\mu_2 A_f}\right]^{-1} \quad (7)$$

where A_f and L_f respectively denote the cross-sectional area and the effective conductive length of the frame.

Note that the thermal transmission efficiency H in (1) should be also corrected by (7). From (4) and (5), reducing pixel's volume or rising thermal conductance help promote thermal response, with the expense of sensitivity degradation.

Part Two—Mechanical Restoring Time: After the IR object is removed, the deformed bimaterial cantilevers will restore due to shearing stresses caused by thermal extension and distribution on the interface between gold (Au) and silicon nitride (SiN_x) layers. The mechanical restoring time can be determined by a dynamic equation, which is described by total bending moments M, rotational inertia J, and angular acceleration ψ [16]

$$\psi(t) = \frac{d^2\theta}{dt^2} = \frac{M}{J} = \frac{w(t_1+t_2)(\alpha_1-\alpha_2)\Delta T}{2Ju} \times \left(1 - \frac{1}{\cosh\left(L\sqrt{\frac{u}{v}}\right)}\right) \quad (8)$$

where w is the width of beams, and t, E, and υ are layer thickness, elastic module, and Poisson's ratio, respectively. u and v are structure constants, and they can be expressed as

$$u = \frac{1}{12}\left(\frac{t_1^2}{B_1} + \frac{t_2^2}{B_2} + \frac{3(t_1+t_2)^2}{B}\right)$$
$$B = B_1 + B_2 = \frac{E_1 t_1^3}{12\left(1-\upsilon_1^2\right)} + \frac{E_2 t_2^3}{12\left(1-\upsilon_2^2\right)}$$
$$v = \frac{2(1+\upsilon_1)}{3E_1} t_1 + \frac{2(1+\upsilon_2)}{3E_2} t_2. \quad (9)$$

Moreover, rotational inertia J can be approximately defined as $J = (1/12)M_L L^2 + (1/4)M_r L^2$, where M_L is a single beam's mass and M_r denotes mass of the reflector and the rest of beams.

From (8), the pixel's mechanical restoring time can be deduced by integration and ψ is proportional to the temperature change. The mechanical restoring time determines the time lag from the moment when the final IR object disappears to the moment when pixels restore to their initial position.

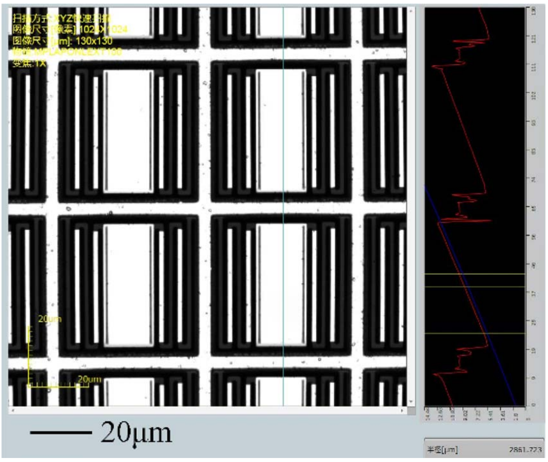

Fig. 2. Picture of bent reflectors made of SiO_2 and Al with radius of curvature of 2862 μm.

III. Design and Optimization

A. Material Selection

To choose ideal materials for the FPA, the following main requirements should be met.

1) The absorber layer has good absorption ability in the range of 8–14 μm.
2) The reflector has high reflectivity in visible spectrum.
3) The large difference in thermal expansion coefficients of two materials is needed.
4) The residual stress in film is easy to regulate to flatten the reflector.

Taking all these requirements into consideration, here, SiN_x and Au were chosen. In fact, the combination of aluminum (Al) and silicon dioxide (SiO_2) should be a better choice. However, due to the difficulties in wet etching and reflector bending caused by residual stress after releasing, it has not been adopted until now. By means of a confocal laser scanning microscope (Olympus OLS4000), an obvious bend (radius of curvature of 2862 μm) of reflectors made of SiO_2 and Al was observed, as shown in Fig. 2. The bend results in the dispersion of diffraction spectrum of the probing light reflected by pixel's reflector into CCD, which degrades the FPA's sensitivity [10].

B. Pixel's Dimension

In this section, we focus on the pixel structure design and optimization to obtain a larger array with smaller pixel size. An ideal design target is to ensure that the pixel size is not larger than 50 μm $\times$ 50 μm. Here, the width of bimaterial cantilevers is set to be 1.5 μm for the purpose of large area of the absorber layer, according to the capability of our lithography technique. Subsequently, the number of folded beams and the thickness of SiN_x and Au are investigated. The calculation results are shown in Fig. 3, where sensitivity $H \times S$ is plotted over the thickness ratio η and folded number n for a fixed value of the pixel area. It illustrates that the folded number has an optimal value of $n = 2$, whereas the thickness ratio of Au to SiN_x, i.e., $\eta = 0.7$, is another optimization value for layer thickness. Technically, thinner SiN_x contributes to bigger sensitivity. However, as an absorber layer, its thickness should be larger than 1 μm to mostly absorb the IR radiation. Because the IR radiation is reflected within the SiN_x layer by the Au layer, SiN_x thickness is set to be 0.5 μm to ensure both absorption and sensitivity. The thickness of the Au layer is defined as 0.2 μm instead of 0.35 μm. It not only reduces the fabrication difficulty in the liftoff process but also alleviates the bending phenomenon of the reflector caused by stress mismatch between Au and SiN_x.

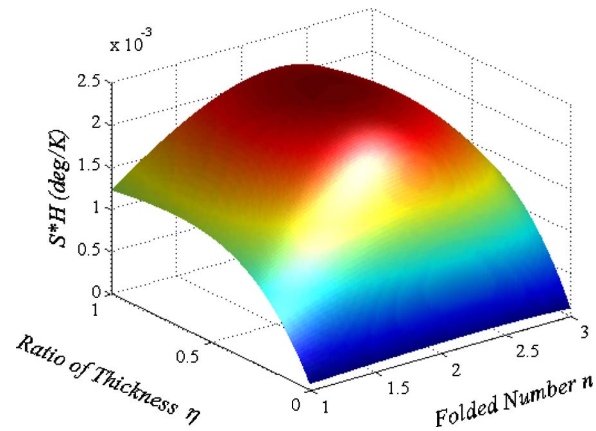

Fig. 3. Theoretical prediction of the FPA's sensitivity, as a function of thickness ratio and folded number, showing that the optimal values are 0.7 and 2, respectively.

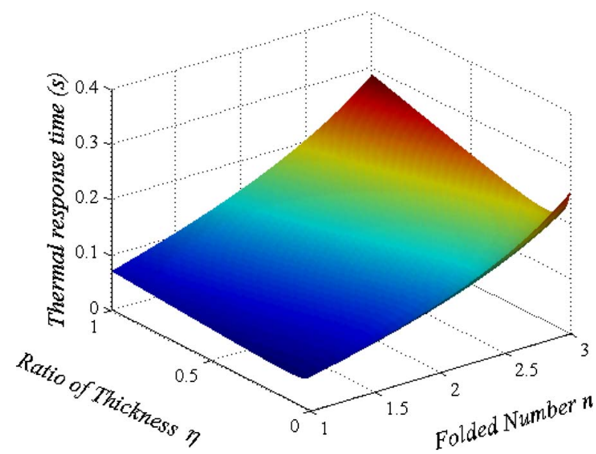

Fig. 4. Theoretical optimization of the thermal response time, as a function of thickness ratio and folded number, showing that the response time is relatively constant while $n \leq 2$.

Fig. 4 shows the thermal response time versus folded number and thickness ratio. When the folded number $n \leq 2$, the thermal response time has a flat tendency to the thickness ratio and increases with increasing folded number. At this time, it is reasonable to think that the response time has no relation with the thickness ratio. For the folded number $n > 2$ and thickness ratio η equal to about 0.1, the response time has a minimum because the total thermal conductance is maximum at that point.

To determine the mechanical restoring time, based on (8), a quotient of ψ divided by the temperature change ΔT is expressed as a function of folded number n and thickness ratio η, which is shown Fig. 5. When keeping the pixel area and ΔT unchanged, the reflector area decreases with the increase in folded number, resulting in the decrease in rotational inertia

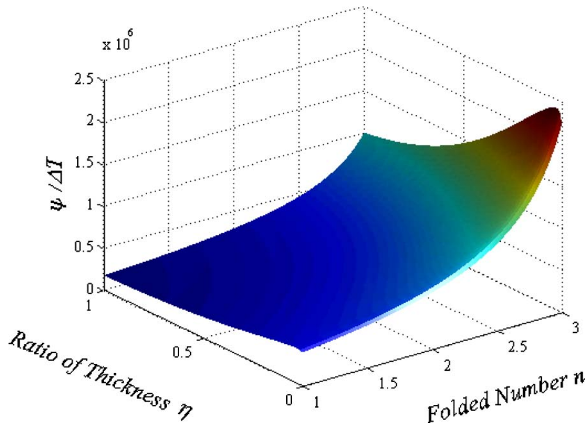

Fig. 5. Pixel's angle acceleration caused by mechanical restoring force. High acceleration shows that FPA has very short mechanical restoring time compared with thermal response time.

TABLE I
OPTIMIZED PARAMETERS FOR FPA

Pixel number	240 x 240
Pixel size(μm)	42 x 42
Folded number	2
Thickness ratio	0.4
Reflector size(μm)	42 x 18
Cantilever width(μm)	1.5
SiNx thickness(μm)	0.5
Au thickness(μm)	0.2

J; in other words, angle acceleration ψ is increased. Raising of $\psi/\Delta T$ with decreasing η can be also attributed to the decrease in J. In addition, the calculated results show that FPA has very quick restoring time (about a few microseconds) because of the high acceleration. Compared with thermal response time (about a hundred microseconds), the mechanical restoring time has very little influence on FPA's response and can be therefore ignored.

Considering the thermal sensitivity and the fabrication limitation (minimum resolvable linewidth is 1.5 μm with a stepper in our laboratory), the final FPA's parameters and pixel's dimensions have been determined and listed in Table I.

Based on the optimized parameters, FPA's performance is calculated as follows:

1) thermal transmission efficiency $H = 3.63\%$;
2) thermomechanical sensitivity $S = 4.69 \times 10^{-2}$ deg/K;
3) thermal sensitivity $R = 20.5$ (gray level/K) based on $\theta_{\min} = 8.33 \times 10^{-5}$;
4) thermal response time $\xi = 121$ ms.

IV. FABRICATION

A. Fabrication Process Flow

After all of the needed parameters have been confirmed, the fabrication process flow is shown in Fig. 6, which includes five main steps.

1) A double-side 0.5-μm SiN_x film was deposited by low-pressure chemical vapor deposition (LPCVD).

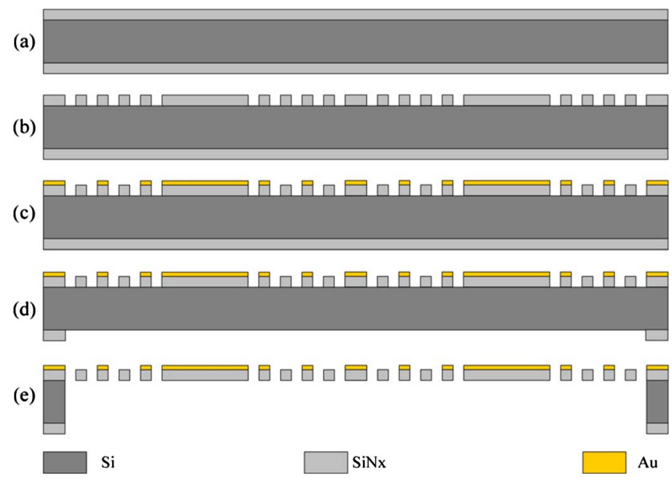

Fig. 6. Sequential process for the fabrication of FPA (only two pixels are illustrated).

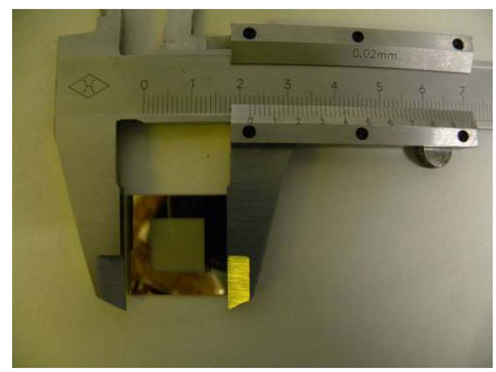

Fig. 7. Fabricated and diced FPA chip with size of 2.2 mm × 2.2 mm.

2) Reactive ion etching was conducted on the top side to remove unwanted SiN_x under the protection of patterned photoresist.
3) A 10-nm chromium adhesive layer and a 0.2-μm Au layer were deposited by electron beam evaporation on the top side after the reflector and beams were patterned.
4) Back-side lithography was conducted to pattern etch window.
5) Silicon substrate beneath pixels was etched away in a KOH solution to form a big and common silicon cup on the back side of a wafer.

Since the pixel's size is about 50 μm $\times$ 50 μm, the corresponding 240 $\times$ 240 FPA's area is about 1.2 mm $\times$ 1.2 mm. Thereby, for the convenience of package, the FPA was diced as a square frame structure with a size of 2.2 mm $\times$ 2.2 mm (see Fig. 7). The diced chip was packaged in a vacuum chamber (see Fig. 8) under air pressure of 0.01 Pa. The vacuum chamber was consisted of a palladium (Pd) alloy for low outgassing rate and an optical glass and a germanium (Ge) glass with high transmissivity for visible light and IR radiation, respectively. From Figs. 7 and 8, one can observe that the FPA has semitransparent effect due to the unmetallized beams and transparent frames between pixels. To obtain an FPA with good performance, two fabrication processes discussed below should be dealt with carefully.

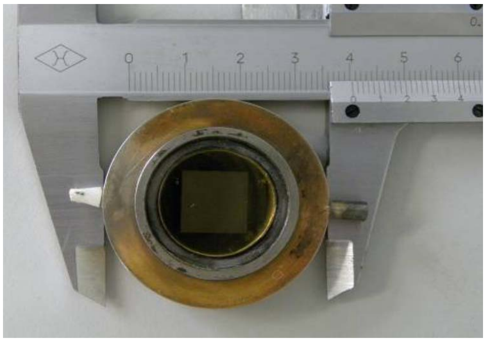

Fig. 8. FPA housed in a vacuum chamber with a diameter of 4 cm and a thickness of 1 cm.

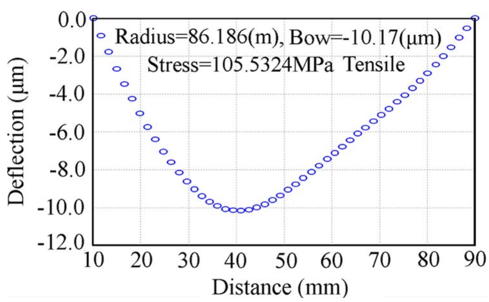

Fig. 9. Nitride film stress on a 4-in wafer after LPCVD, showing 105.5 MPa of tensile stress.

B. Stress Control of SiN_x Film

Since a SiN_x film is selected as the absorption/structure layer, the quality of the SiN_x film has an important influence on FPA's performance. Our earlier experiments showed that if the residual stresses in the SiN_x film are too high, similar to the case of combination of SiO_2 and Al mentioned in Section III, it is difficult to fabricate a flat reflector for FPA. On the other hand, if the SiN_x film has compressive stresses, wrinkles could occur after the substrate is removed and the film is released. By controlling the gas flow ratio, $SiH_2Cl_2 : NH_3$, to be 3, depositing temperature of about 940 °C and vacuum of about 10^{-3} Pa, a low-stress SiN_x film was deposited on 4-in wafers in our LPCVD machine. The film stress distribution was shown in Fig. 9 (measured by Flexus 2320). Low tensile stress of about 100 MPa was obtained.

C. Wet Etching and Release

For the freestanding structure, silicon substrate beneath pixels is entirely removed by using wet etching in a hot 33% KOH aqueous solution (in weight ratio) at 80 °C. The wet etching process can be described by a reaction equation

$$Si + H_2O + 2KOH = K_2SiO_3 + 2H_2 \uparrow . \qquad (10)$$

On one hand, hydrogen is produced, which caused massive bubbles to continuously impact pixels during the etching progress; on the other hand, when silicon beneath the SiN_x film is being etched, pixels become more and more fragile and very easy to be damaged by the hydrogen bubbles or any disturbing of solution. Fig. 10 shows damaged pixels during wet etching, resulting in dead pixels on the final detected IR image.

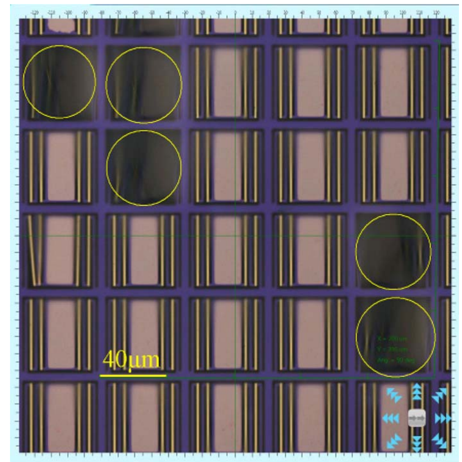

Fig. 10. FPA's damaged pixels after wet etching. The circles indicated the damaged pixels.

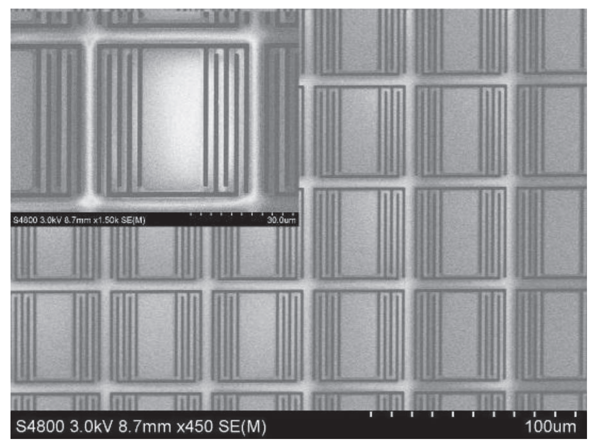

Fig. 11. SEM picture of fabricated FPA with thickness of 0.2-μm Au and 0.5-μm SiN_x. An amplified pixel is shown at the top left.

To minimize the damage, single-side etching process and two-step method are employed. The top side of the wafer is covered by anti-etch glue (Crystalbond 509, Structure Probe, Inc.). Therefore, etching reaction will only happen from the bottom side (i.e., the silicon substrate side). For the two-step method, the etching process will stop at the point where silicon substrate remains about 30-μm-thick silicon at 80 °C. Then, we lower down the temperature of the KOH solution to room temperature and continue the etching procedure until residual silicon is fully removed. Finally, a successfully fabricated FPA is presented in Fig. 11.

V. EXPERIMENTS AND MEASUREMENTS

Fig. 12 shows the principle schematic and experimental setup of the uncooled FPA IR imaging detector with an optical readout system.

On one hand, the incident IR radiation from the objective is focused by an IR lens and illuminated the back side of the FPA housed in a vacuum chamber. The image intensity from the reflectors will change due to cantilevers bending, which

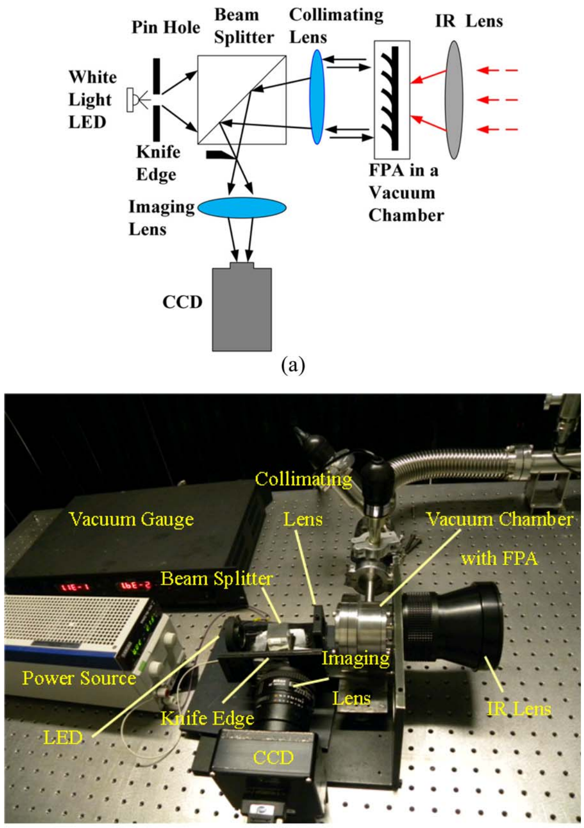

Fig. 12. (a) Schematic and principle of the experiment. (b) Experimental setup of our FPA IR imaging system.

changes the direction of the reflected readout light. On the other hand, visible light from a light-emitting diode (LED) passes through a pinhole and is collimated to illuminate the front side of the FPA, for the purpose of simultaneous measurement of the deflections of all cantilever beams. The light reflected from the FPA creates a thermal image, passes through a knife-edge filter, and is collectively projected onto a 12-bit CCD by an imaging lens. To obtain an IR image, we precaptured the background image without IR stimulus, then we subtracted the background from an image with IR stimulus. The knife-edge filter is used to optimize the optical detecting sensitivity, which is placed at the center position of the zeroth-order spectra of reflectors to let half fluxes pass through, and the readout illumination should make the CCD approach its full measuring range.

All experiments and measurements were performed with this system with an f/0.8 IR lens and a 12-bit CCD at the background temperature of 25 °C. In addition, the FPA was packaged in a vacuum chamber under air pressure of 1×10^{-2} Pa except the section of air pressure test.

A. Thermal Imaging Results

A person wearing glasses is about 2 m away from the IR lens and raising his both hands was detected by the system, as shown in Fig. 13(a). Compared with our previous result shown in Fig. 13(b), significant improvements in image resolution can be observed, and the FPA's performance has been also improved.

Fig. 13. Human's IR image detected by the FPA with (a) current design and (b) previous design.

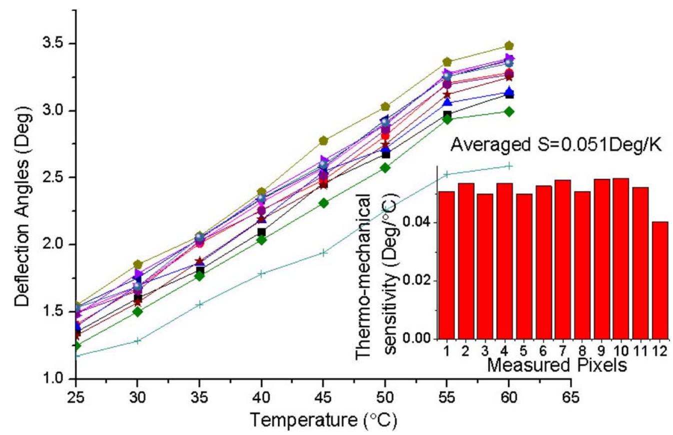

Fig. 14. Thermomechanical sensitivity of 12 different pixels, showing the averaged thermal–mechanical sensitivity $S = 0.051$ Deg/k.

B. Measurements on Thermomechanical Sensitivity

Thermomechanical sensitivity S is an essential parameter to estimate the FPA's performance. The dependence of temperature has been measured for the deflection angles with 12 random pixel's reflectors. The temperature is controlled by an adjustable hot plate. The deflection angle is detected by a confocal laser scanning microscope (Olympus OLS4000). Based on the measurement data, thermomechanical sensitivity S has been obtained and plotted in Fig. 14. By averaging those 12 sets of data, the experimental results indicate that the fabricated FPA's thermomechanical sensitivity is 0.051 deg/K.

C. FPA's Thermal Sensitivity

To obtain thermal sensitivity R, the pixel's gray response to the temperature rise has to be measured. The accuracy of temperature is about 0.01 K for the adjustable IR source. CCD's gray responses caused by stochastic 20 different pixels at each temperature from 25 °C to 50 °C by step of 1 °C have been taken and averaged. Fig. 15 shows the averaged experimental gray responses of the 20 pixels versus temperature changes. The differences of gray responses result from the nonuniformities among pixels. The thermal sensitivity is about 21.4 gray level/K by averaging the responses of those 20 pixels.

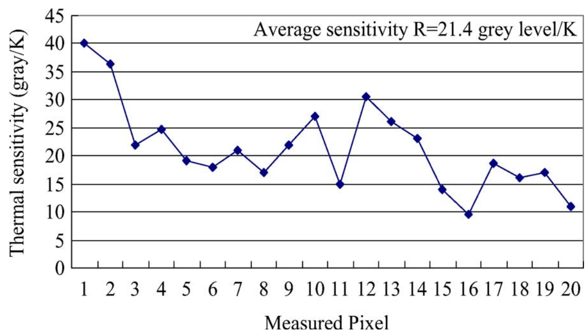

Fig. 15. Thermal sensitivity of 20 different pixels, showing the averaged thermal sensitivity $R = 21.4$ gray level/K.

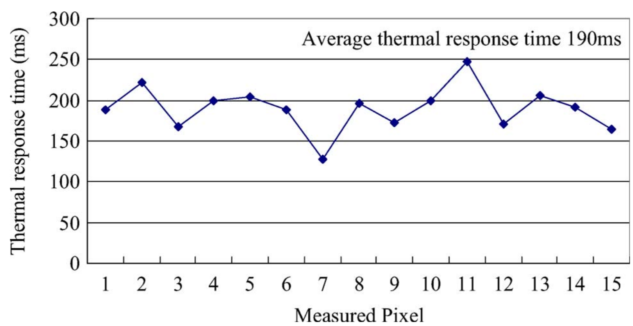

Fig. 16. Thermal response time of 15 pixels, showing the averaged thermal response time of 190 ms.

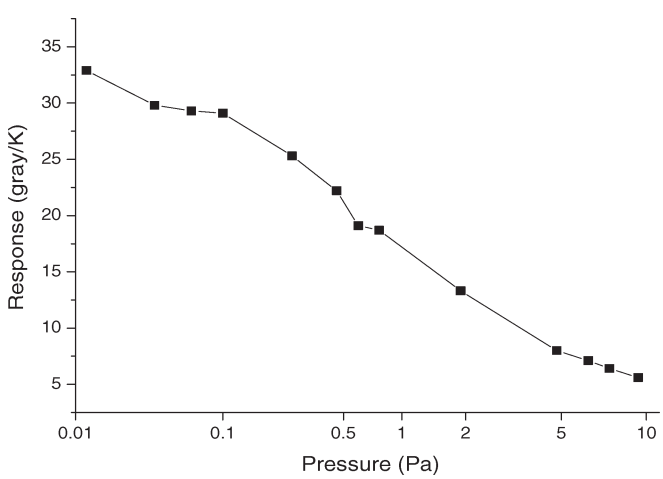

Fig. 17. Relationship between air pressure and thermal sensitivity. When the air pressure is 1 Pa, the FPA's thermal sensitivity dropped by more than 50%.

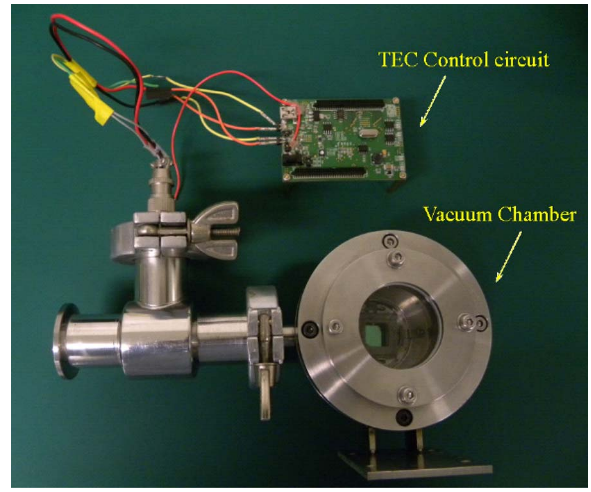

Fig. 18. Experimental setup to estimate the frame's thermal conductance at different temperatures in a low-pressure vacuum chamber with TEC.

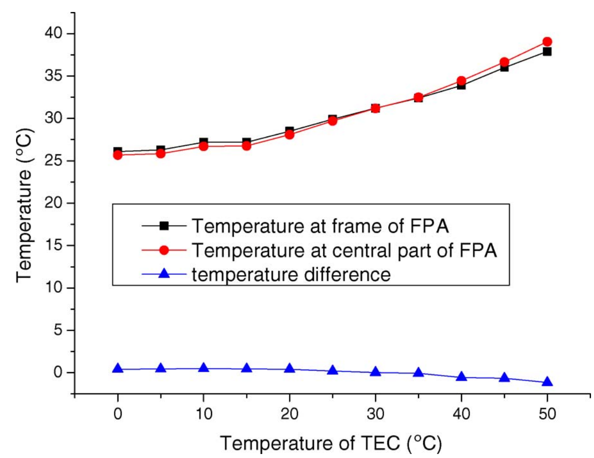

Fig. 19. Temperature difference between the frame and central part of FPA. The very small difference shows that heat can be conducted by the frame at a low air pressure of 0.75 Pa.

TABLE II
COMPARISON OF CALCULATED AND EXPERIMENTAL RESULTS

	calculation	experiment
H	3.63%	-
S (deg/K)	4.69×10^{-2}	5.1×10^{-2}
R (gray level/K)	20.5	21.4
ξ (ms)	121	190
NETD(mK)	390	373

D. NETD Estimation

NETD is often used to define the sensitivity performance of an IR imaging system. It specifies the minimum detectable temperature difference and is described as a ratio of minimum detectable signal to the system noise. Thus, our MEMS FPA's NETD can be expressed as

$$\mathrm{NETD} = I_n/R \tag{11}$$

where I_n is the total noise of the optical readout system, which is caused by the temperature fluctuation, thermomechanical fluctuation, optical readout noise induced by the instability of probing light source, and noise of CCD caused by the dark current or the analog-to-digital conversion circuit. To determine the system noise, with the absence of IR object, 300 thermal images have been continuously captured by CCD, then statistic noise variance has been calculated; thus, the mean square of system noise of $I_n = 8$ gray level has been obtained. According to (11) and thermal sensitivity R measured before, the NETD has been calculated for about 373 mK. Compared with that of our previous design, i.e., 330 mK, no statistically significant increase in NETD was observed.

NETD depends on the thermomechanical sensitivity and system noise. Theoretically, the NETD can reach 5 mK by increasing the thermal–mechanical response and decreasing the system noise [3].

TABLE III
COMPARISON OF TWO GENERATIONS OF FPA

	Array number	Pixel size (μm²)	NETD (mK)	Fill factor	Readout method
Our previous	160×160	60×60	330	30.8%	optical
Our present	240×240	42×42	373	30.9%	optical
D.Grbovic [4]	256×256	75×75	<500	62%	optical
X. Yu [5]	160×120	146×110	60(estimated)	29.8%	optical
Hideo Wada	256×256	50×50	150	51%	electrical

E. Thermal Response Time

Thermal response time has been also measured. When an IR object comes up, the time-varying CCD's gray levels are immediately acquired by a data acquisition card and then processed by a computer program to calculate the response time. Fifteen random pixels were selected to measure the thermal response. Based on the measured data shown in Fig. 16, the averaged thermal response time has been calculated to be 190 ms.

F. Influence of Air Pressure

The air influence on the FPA's performance can be ignored in the theoretical analysis aforementioned. From (1) and (4), it is easy to find that air convection and conduction can reduce FPA's thermal sensitivity R. To investigate the influence of air pressure on the FPA's performance, we measured thermal sensitivity R versus air pressure, as shown in Fig. 17. As the air pressure increases and reaches about 1 Pa, R drops more than 50% and since then has sharply fallen as air pressure continues to rise.

G. Influence of Frame's Thermal Conduction

To estimate thermal conduction of pixel's frame and verify the validity of (7), an experiment has been conducted by using a thermal electronic cooler (TEC), which has the same frame shape corresponding to the diced FPA. To minimize the influence of air, the TEC and FPA were together packaged in a vacuum chamber at a pressure of 7.5×10^{-1} Pa. The experimental setup is shown in Fig. 18.

At background temperature of 30 °C, by adjusting TEC's temperature from 0 °C to 45 °C by a step of 5 °C, temperatures of the frame and central part of the FPA have been respectively measured with a commercial IR camera (FLIR A350) and plotted in Fig. 19. The quite small temperature differences between the frame and central part of the FPA indicate that heat can be conducted by the frame between neighboring pixels under vacuum environment. Therefore, the frame's conductance must be considered in the design carefully.

Finally, Table II summarizes a comparison of the calculated and measured results. In addition, the implementation results from a few reported FPAs are compared in Table III. It is obvious that our device has a sharp improvement on resolution with NETD of about 373 mK. It should be noted that the present minimum resolvable linewidth of photolithography is 1.5 μm. According to the Rayleigh's resolution criterion, the width of bimaterial cantilevers can be further reduced with increasing the numerical aperture of the projection system or decreasing the wavelength of the exposure light.

VI. CONCLUSION

In summary, based on an optical readout system, we have demonstrated a 240 $\times$ 240 MEMS uncooled IR FPA with 42-μm pitch pixels. An improved analytical tool has been presented, and the optimization of the design parameters, including thermal transmission efficiency, thermomechanical sensitivity, thermal sensitivity, and response time, has been studied. The obtained IR FPA was characterized in terms of thermomechanical sensitivity, thermal sensitivity, NETD, thermal response time, and air pressure of the vacuum chamber. Compared with our previous results, the number of the fabricated FPA's pixels has increased by 125%, and the corresponding pixel's area has decreased by 51%. Furthermore, our FPA has a good sensitivity with NETD of about 373 mK. With future lithography tool employing larger numerical aperture of the projection system or smaller wavelength of the exposure light, the pixel's size and array number will improve accordingly.

REFERENCES

[1] H. Wada and M. Nagashima, "Design and performance of 256X256 bolometer-type uncooled infrared detector," in *Proc. SPIE*, 1998, vol. 3379, pp. 90–100.

[2] J. L. Tissot, B. Fièque, C. Trouilleau, P. Robert, A. Crastes, C. Minassian, and O. Legras, "640 $\times$ 480 uncooled amorphous silicon IRFPA with 25 μm pixel-pitch," in *Proc. SPIE*, 2006, vol. 6206, pp. 620618-1–620618-4.

[3] Y. Zhao, M. Mao, R. Horowitz, A. Majumdar, J. Varesi, P. Norton, and J. Kitching, "Optomechanical uncooled infrared imaging system: Design, microfabrication, and performance," *IEEE J. Microelectromechan. Syst.*, vol. 11, no. 2, pp. 136–146, Apr. 2002.

[4] S. R. Hunter, G. S. Maurer, G. Simelgor, S. Radhakrishnan, J. Gray, K. Bachir, T. Pennell, M. Bauer, and U. Jagadish, "Development and optimization of microcantilever based IR imaging arrays," in *Proc. SPIE*, 2008, vol. 6940, no. 2, pp. 694013-1–694013-12.

[5] N. Lavrik, R. Archibald, D. Grbovic, S. Rajic, and P. Datskos, "Uncooled MEMS IR imagers with optical readout and image processing," in *Proc. SPIE*, 2007, vol. 6542, pp. 65421E-1–65421E-8.

[6] D. Grbovic, N. V. Lavrik, P. G. Datskos, D. Forrai, E. Nelson, J. Devitt, and B. McIntyre, "Uncooled infrared imaging using bimaterial microcantilever arrays," *Appl. Phys. Lett.*, vol. 89, no. 7, pp. 073118-1–073118-3, Aug. 2006.

[7] X. Yu, Y. Yi, S. Ma, M. Liu, X. Liu, L. Dong, and Y. Zhao, "Design and fabrication of a high sensitivity focal plane array for uncooled IR imaging," *J. Micromech. Microeng.*, vol. 18, no. 5, p. 057001, May. 2008.

[8] C. Li, B. Jiao, S. Shi, D. Chen, T. Ye, Q. Zhang, Z. Guo, F. Dong, and Z. Miao, "A novel uncooled substrate-free optical-readable infrared detector: Design, fabrication and performance," *Meas. Sci. Technol.*, vol. 17, no. 7, pp. 1981–1986, Jul. 2006.

[9] F. Dong, Q. Zhang, D. Chen, Z. Miao, Z. Xiong, Z. Guo, C. Li, B. Jiao, and X. Wu, "Uncooled infrared imaging device based on optimized optomechanical micro-cantilever array," *Ultramicroscopy*, vol. 108, no. 6, pp. 579–588, May 2008.

[10] T. Cheng, Q. Zhang, B. Jiao, D. Chen, and X. Wu, "Optical readout sensitivity of deformed microreflector for uncooled infrared detector: Theoretical model and experimental validation," *J. Opt. Soc. Amer. A, Opt. Image Sci.*, vol. 26, no. 11, pp. 2353–2361, Nov. 2009.

[11] M. Liu, Y. Zhao, X. Liu, X. Yu, X. Wang, and T. Li, “Shape distortions of infrared focal plane array and optical readout,” in *Proc. SPIE*, 2008, vol. 6621, pp. 66211H-1–66211H-11.
[12] Z. Guo, Q. Zhang, F. Dong, D. Chen, Z. Xiong, Z. Miao, C. Li, B. Jiao, and X. Wu, “Performance analysis of microcantilever arrays for optical readout uncooled infrared imaging,” *Sens. Actuators A, Phys.*, vol. 137, no. 1, pp. 13–19, Jun. 2007.
[13] P. W. Kruse, “Principles of uncooled infrared focal plane arrays,” in *Semiconductors and Semimetals*. San Diego, CA: Academic, 1997, pp. 17–42.
[14] J. Lai, T. Perazzo, Z. Shi, and A. Majumdar, “Optimization and performance of high-resolution micro-optomechanical thermal sensors,” *Sens. Actuators A, Phys.*, vol. 58, no. 2, pp. 113–119, Feb. 1997.
[15] Z. Miao, Q. Zhang, D. Chen, Z. Guo, F. Dong, Z. Xiong, X. Wu, C. Li, and B. Jiao, “Uncooled IR imaging using optomechanical detectors,” *Ultramicroscopy*, vol. 107, no. 8, pp. 610–616, Aug. 2007.
[16] E. Sutiir, “Stresses in bi-metal thermostats,” *J. Appl. Mech.*, vol. 53, no. 3, pp. 657–660, Sep. 1986.

Yi Ou received the B.S. and Ph.D. degrees in physics from Beijing Institute of Technology, Beijing, China, in 1997 and 2003, respectively.

From 2010 to 2011, he was a Visiting Scholar in the School of Electronics and Computer Science, University of Southampton, Southampton, U.K. He is currently with the Key Laboratory of Microelectronics Devices and Integrated Technology, Institute of Microelectronics, Chinese Academy of Sciences, Beijing. His research interests include the design and fabrication of microelectromechanical systems sensors and actuators.

Zhigang Li received the M.A.Sc. degree in microelectronics from the Graduate University of the Chinese Academy of Sciences (CAS), Beijing, China, in 2007.

He is currently with the Institute of Microelectronics, CAS, which he joined upon the completion of his M.A.Sc. studies. He was a Visiting Scholar in the Nanoelectronics Fabrication Facility, The Hong Kong University of Science and Technology, from February 2009 to February 2010. His research area is a MEMS-based thermal imaging technique with optical readout.

Fengliang Dong received the B.Tech. degree from Hefei University of Technology, Hefei, China, in 2002 and the Ph.D. degree from the University of Science and Technology of China, Hefei, in 2007.

From April 2008 to March 2011, he was with INESC Microsistemas e Nanotecnologias (INESC MN), Lisbon, Portugal, as a Postdoctoral Researcher. He is currently with the National Center for Nanoscience and Technology, Beijing, China. His research area includes e-beam lithography, thin-film MEMS/NEMS, and nanoscale devices.

Dapeng Chen received the M.S. and Ph.D. degrees in physics from the University of Science and Technology of China, Hefei, China, in 1995 and 1998, respectively.

He is a Professor in the Key Laboratory of Microelectronics Devices and Integrated Technology, Integrated Circuit Advanced Process Center, Institute of Microelectronics, Chinese Academy of Sciences, Beijing, China. He is teaching and conducting research in the areas of microelectromechanical systems and complementary metal–oxide–semiconductor technology.

Qingchuan Zhang received the B.S. and M.S. degrees in mechanical systems from the University of Science and Technology of China (USTC), Hefei, China, in 1984 and 1987, respectively, and the Ph.D. degree from Saitama University, Saitama, Japan.

He is currently a Professor in the CAS Key Laboratory of Mechanical Behavior and Design of Materials, USTC. His research interests range from MEMS and infrared imaging to optical measurement.

Changqing Xie was born in China in 1971. He received the B.S. degree in physics from the University of Science and Technology of China, Hefei, China, in 1993.

He is currently a Professor with the Institute of Microelectronics, Chinese Academy of Sciences, Beijing, China. He has authored or coauthored 98 papers in peer-reviewed journals. His current research works focus on design, fabrication, testing, and applications of diffractive optical elements.

Dr. Xie was the recipient of the 2003, 2006, and 2010 Beijing science and technology progress first prize, the 2010 Ministry-based second prize, and the 2008 “863 outstanding topics” award. He is currently a Senior Member of the Chinese Optical Society.